

Physical prior guided cooperative learning framework for joint turbulence degradation estimation and infrared video restoration

Ziran Zhang^a, Yuhang Tang^b, Zhigang Wang^b, Yueting Chen^{a,*}, Bin Zhao^b

^a*State Key Laboratory of Extreme Photonics and Instrumentation, College of Optical Science and Engineering, Zhejiang University, Hangzhou, 310027, China*

^b*School of Artificial Intelligence, OPTics and ElectroNics (iOPEN), Northwestern Polytechnical University, Xi'an, 710072, China*

Abstract

Infrared imaging and turbulence strength measurements are in widespread demand in many fields. This paper introduces a Physical Prior Guided Cooperative Learning (P²GCL) framework to jointly enhance atmospheric turbulence strength estimation and infrared image restoration. P²GCL involves a cyclic collaboration between two models, *i.e.*, a TMNet measures turbulence strength and outputs the refractive index structure constant (C_n^2) as a physical prior, a TRNet conducts infrared image sequence restoration based on C_n^2 and feeds the restored images back to the TMNet to boost the measurement accuracy. A novel C_n^2 -guided frequency loss function and a physical constraint loss are introduced to align the training process with physical theories. Experiments demonstrate P²GCL achieves the best performance for both turbulence strength estimation (improving C_n^2 MAE by 0.0156, enhancing R^2 by 0.1065) and image restoration (enhancing PSNR by 0.2775 dB), validating the significant impact of physical prior guided cooperative learning.

Keywords: Atmospheric turbulence, Infrared imaging, Cooperative learning

*Corresponding author

Email address: chenyt@zju.edu.cn (Yueting Chen)

1. Introduction

Infrared imaging and turbulence strength (TS) measurements are increasingly recognized for their scientific and technical value across a diverse range of fields[1, 2]. Infrared imaging is pivotal for its ability to capture images based on thermal emissions from objects, making it indispensable in situations where visibility is impaired by darkness, fog, or smoke. Similarly, the measurement of TS is crucial for understanding atmospheric dynamics, improving flight safety by predicting air turbulence, and enhancing weather forecasting accuracy. As such, both technologies play a vital role in advancing scientific research, and ensuring public safety, thereby underscoring their growing importance and widespread utility in contemporary society.

The quality of thermal infrared imaging can be affected by atmospheric turbulence, which is caused by fluctuations in the refractive index of airflows due to temperature changes and accumulation over long distances. This often leads to image blur and distortion, especially when imaging distant targets. As a result, subsequent image analysis and application become more challenging. However, measuring TS has proven to be valuable not only for laser communications[3], astronomical observations[4], and optics-driven drones[5] but also for the restoration of infrared images[6]. In image restoration tasks, TS can be used as prior knowledge to reduce the negative effects of turbulence. The intensity of turbulence(C_n^2) reflects the time-averaged Fourier phase distortion in the imaging process. Furthermore, the restored images can also serve as a reference for predicting atmospheric TS since the turbulence degradation is stochastic and a reference is needed. Considering that these two tasks are physically complementary, this paper attempts to design an innovative cooperative learning framework to achieve mutual enhancement between them.

Traditional methods for measuring atmospheric turbulence, such as Doppler radar[7], laser transmission[8], and temperature fluctuation techniques[9], are costly and intricate. In contrast, a method has recently emerged, utilizing a deep learning-based approach for deducing TS from images[10]. Despite this, this emerging approach inadequately captures the two-dimensional(2D) turbulence field that is essential for describing image degradation. Concurrently, image restoration research utilizing deep learning fails to incorporate TS effectively during training and inference[11, 12], despite its potential benefits. Moreover, the integration of TS into deep learning-based image restoration processes[6] has yet to be fully optimized, leaving room for improvement.

Recognizing these gaps, our work aims to introduce a framework that not only enhances the accuracy of 2D TS measurement but also leverages turbulence information more effectively in image restoration tasks, thereby overcoming the limitations of current methodologies. Our paper presents three key contributions:

1. **Dual-Model Cooperative Learning Framework:** The P²GCL framework introduces a dual-model approach, integrating TMNet for TS measurement and physical prior provision, alongside TRNet for infrared image sequence restoration and TS prediction referencing. This setup promotes a synergistic enhancement of TS measurement and image restoration through cooperative learning.
2. **Innovative C_n^2 -Guided Training Approach:** A novel C_n^2 -guided frequency loss function is proposed to guide the training of the cooperative learning framework. The integration of the 2D Fourier Transform enhances the global awareness of the image restoration network, aligning it with optical diffraction theory, while guidance from C_n^2 boosts its local perception capabilities. Moreover, the collaboration between $L_{C_n^2}$ and L_{physic} in the loss function enhances the framework’s physical interpretability.
3. **Efficient Transformer Integration for Feature Reconstruction:** The addition of efficient transformer blocks to P²GCL significantly improves feature reconstruction and infrared image sequence processing. Experiments demonstrate P²GCL achieves the best performance for both TS estimation (improving C_n^2 MAE by 0.0156, enhancing R^2 by 0.1065) and image restoration (enhancing PSNR by 0.2775 dB).

2. Related Works

Prior-guided Image Restoration. Recently, incorporating prior knowledge to guide image restoration has shown great effectiveness. Explicit shape priors help resolve ambiguities during deblurring[13] and super-resolution[14]. Low-rank assumptions make use of repetitive patterns for inpainting[15] and compression artifact reduction[16]. More structural priors through learning also benefit dehazing [17] and deraining[18]. Advancements have also been made by leveraging turbulence priors to enhance infrared image restoration outcomes[6]. These works on prior-driven image processing and collaborative effects between tasks hold great potential for future exploration.

Atmospheric Turbulence Strength Measurement. Hardware-based TS measurement methods, including Doppler radar[7], laser transmission[8] and temperature fluctuation techniques[9], have been utilized to measure atmospheric TS. However, these methods require expensive and complex instrumentation to obtain spatially integrated turbulence measurements over limited distances. A recent deep learning method have shown potential for rapid and accurate TS prediction directly from images[10], without hardware enhancements. However, this method can only estimate a single-point value of turbulence, failing to capture the spatial variations across the image area.

Turbulence Degradation Removal. Classical image processing algorithms, such as variational approaches[19]. Unfortunately, the intricate optimization problems posed lead to high computational complexity and slow convergence. This has limited their real-time performance. Recent deep learning approaches have exhibited potential for accurate turbulence mitigation without extra hardware[20]. Adversarial networks can synthesize visually appealing restorations[11, 21], while transformers show promise in more realistic reconstructions[22, 12]. Physics-driven simulations have also enabled realistic turbulence generation[23, 24]. However, challenges remain in terms of artifact reduction and physical interpretability increase. More broadly, integrating physical priors to guide unified cooperative designs can progress beyond these limitations for joint infrared image sequence restoration and 2D turbulence mapping.

3. Physical principle

3.1. Atmospheric Turbulence Image Degradation Model

Addressing atmospheric turbulence-induced image degradation, especially in infrared imaging, involves modeling the process through Fresnel diffractions and Kolmogorov phase distortions[25]. To simplify the complex inverse problem, we approximate turbulence effects as the following equation:

$$\tilde{I} = (\mathcal{H} \circ \mathcal{G})(I) + N = \mathcal{T}(I) + N. \quad (1)$$

where \tilde{I} is the observed image, \mathcal{H} is the spatial blur, \mathcal{G} is the pixel displacement, N is the noise, and \mathcal{T} is the combined effect of \mathcal{H} and \mathcal{G} on the original image I . This model shows how turbulence can degrade infrared imaging, emphasizing the challenges and opportunities in this field. Infrared imaging is sensitive to turbulence caused by temperature variations, which can

cause grayscale drifts. This makes it crucial for observing and measuring turbulence effects. To address this issue, we propose a method that jointly estimates the physical prior of the degradation model \mathcal{T} and reconstructs the clean image from the degraded one.

3.2. TS Measurement via Infrared Imaging

The strength of the turbulence can be measured using two constants: the atmospheric refractive index structure constant (C_n^2) and the temperature structure constant (C_T^2). These constants are related by the following equation[9]:

$$C_n^2 = \left(k \frac{P}{T^2}\right)^2 C_T^2, \quad (2)$$

where k is a constant 79×10^{-6} , P represents the local atmospheric pressure and T represents temperature. C_T^2 represents temperature variations correlated with TS. C_T^2 can be defined as follows[9]:

$$C_T^2 = \langle [T(x) - T(x + d)]^2 \rangle d^{-\frac{2}{3}}, \quad (3)$$

where x is the position, d is the distance, $\langle \cdot \rangle$ denote the time average. Planck's Law specifies the spectral radiance for a body at a given wavelength, which varies with temperature, particularly in the context of infrared imaging, where not all wavelengths are considered. Integrating the spectral radiance within the infrared range yields a form of the Stefan-Boltzmann Law, which correlates the total emitted infrared radiance to the fourth power of the body's temperature, adjusted for emissivity and the Stefan-Boltzmann constant:

$$T = \left(\frac{M}{\epsilon\sigma}\right)^{\frac{1}{4}}, \quad (4)$$

where M represents the radiant exitance, ϵ represents the emissivity of the surface, σ represents the Stefan-Boltzmann constant. Generally, the grayscale of pixels in thermal infrared imaging devices is assumed to be linearly correlated with the temperature of the imaged target. Furthermore, thermal infrared imaging equipment is sensitive to temperature changes, which can lead to grayscale drifts in the imaging process due to heat fluctuations in turbulent environments. These characteristics make thermal infrared imaging a suitable way to measure turbulence.

4. P²GCL Framework

Since thermal infrared imaging is suited for measuring turbulence priors and prior knowledge can aid infrared image restoration, a new P²GCL framework has been proposed. There are two models involved in the framework, TMNet and TRNet:

$$\text{P}^2\text{GCL: } \begin{cases} O_{TS} = \text{TMNet}(S_{turb}, \text{None}), \\ S_{rest} = \text{TRNet}(S_{turb}, O_{TS}), \\ O_{TS} = \text{TMNet}(S_{turb}, S_{rest}), \end{cases} \quad (5)$$

where O_{TS} represents the TS prior, S_{turb} represents the turbulence image sequences, and S_{rest} represents the restored image sequences. TMNet can estimate the strength of atmospheric turbulence. It has two input modes: single and dual input mode. In the single input mode, TMNet can predict TS without using a reference image. However, the dual input mode provides more accurate results. To enable the dual input mode, TRNet utilizes the TS prior generated by TMNet in the single mode and restores the S_{turb} . The restored S_{rest} is used as references of the S_{turb} and fed back to TMNet. The final TS field is generated by the TMNet in dual input mode.

As shown in Fig. 1, TMNet and TRNet process videos consisting of 15-frame images. The reference image is derived from image sequences through channel average pooling, allowing single-mode TMNet to operate independently of TRNet. Both TMNet and TRNet employ 3D convolution blocks as feature extractors. The baseline for our model is established on the PBCL[6] framework. Consequently, both the feature extraction component and the coordinate attention mechanism in our model are consistent with those implemented in PBCL. To reconstruct 2D TS fields and infrared image sequences, we introduce two advanced transformer-based reconstructors incorporating Channel Transposed Self-Attention(CTSA) and Gated Feedforward Neural Network(GFN).The architecture of the 2D reconstructor is shown in Fig.2. The 3D reconstructor uses the 2D reconstructor as its foundational module and processes frames through the 2D mechanism. These reconstructors utilize efficient transformer blocks for improved performance, complemented by upsampling layers to enhance feature resolution. The CTSA mechanism addresses the high computational and memory costs associated with traditional self-attention in high-resolution images by applying self-attention across channels rather than spatial dimensions. This method significantly

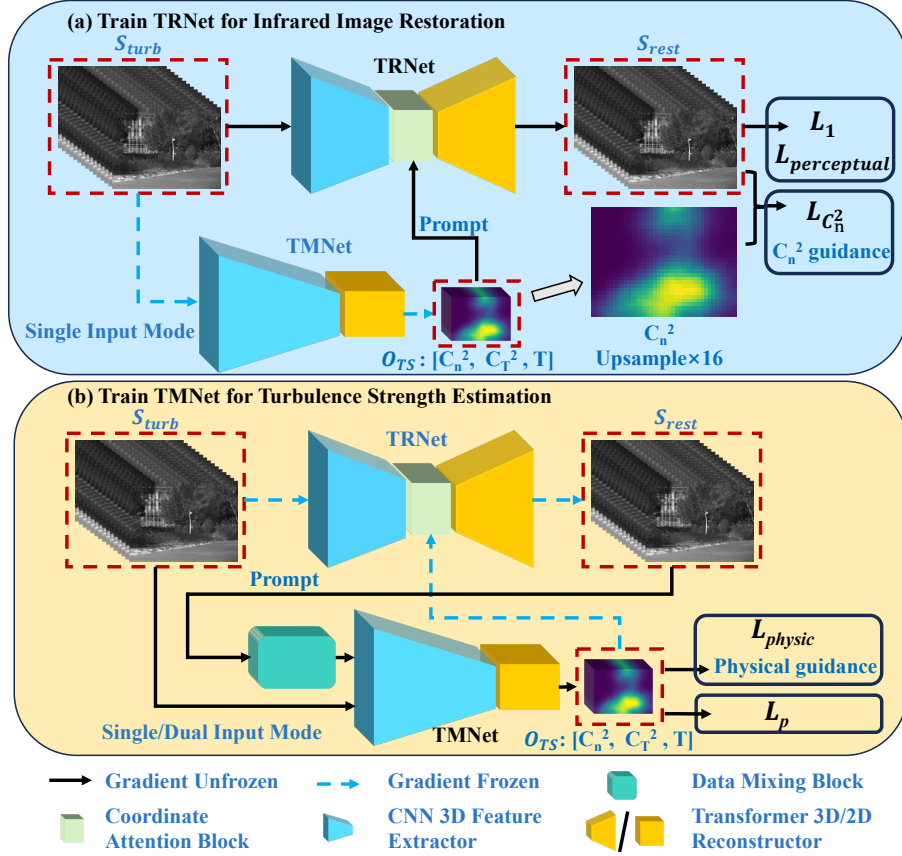


Figure 1: The Physical Prior Guided Cooperative Learning (P²GCL) framework’s training process with TRNet for infrared image restoration (a) and TMNet for turbulence strength(TS) estimation (b), highlighting the iterative training cycle between the two networks.

reduces complexity from quadratic to linear, as follows:

$$\mathbf{A} = \text{Softmax} \left(\frac{\mathbf{K}^T \mathbf{Q}}{\sqrt{d_k}} \right) \mathbf{V}, \quad (6)$$

where \mathbf{Q} , \mathbf{K} , and \mathbf{V} are the query, key, and value matrices generated through 1×1 convolutions for pixel-wise cross-channel context and 3×3 depth-wise convolutions for channel-wise spatial context, reducing the dimensionality of attention maps and focusing on capturing global context through cross-covariance across channels. GFN enhances feature transformation by introducing a gating mechanism and depth-wise convolutions within the feed-

forward network, emphasizing local context for effective restoration. First, the input \mathbf{X} is processed as follows:

$$Y_1 = \sigma(W_{d1} * (W_{p1} * \text{LN}(\mathbf{X}))) \quad (7)$$

$$Y_2 = W_{d2} * (W_{p2} * \text{LN}(\mathbf{X})) \quad (8)$$

where σ denotes the GELU function. These processed outputs Y_1 and Y_2 are then combined and further processed:

$$\hat{\mathbf{X}} = \mathbf{X} + W_{p0} * (Y_1 \odot Y_2) \quad (9)$$

where W_{p0} , W_{p1} , and W_{p2} represent point-wise convolutional filters; W_{d1} and W_{d2} denote depth-wise convolutional filters, and \odot indicates element-wise multiplication. This approach leverages LN (layer normalization) and σ (GELU) to modulate the flow of information, providing a balance between global and local information processing within the network.

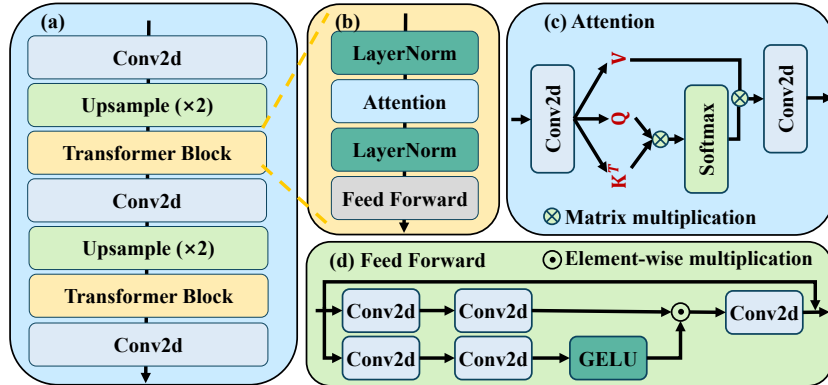


Figure 2: Transformer Reconstructor. (a) Detailed structure of the Transformer 2D reconstructor. (b) Transformer block (c) Multi-Dconv Head Transposed Attention (CTSA) (d) Gated-Dconv Feed-Forward Network (GFN).

CTSA and GFN synergize within the transformer blocks to facilitate spatial self-attention and feature transformation, effectively processing the spatial-temporal dynamics of video sequences. The enhanced transformer block, utilizing spatial self-attention, applies attention weights to the feature map, now augmented with advanced mechanisms for handling both global and local contexts. In the 3D Transformer reconstructor, adjacent frames

assist in the middle frame’s restoration, leaving the first two and last two frames without auxiliary frames, resulting in an 11-frame output sequence. Despite this, the approach’s design ensures that multiple inferences do not compromise the final video quality.

5. P²GCL Training Strategy

5.1. Global awareness of Fourier transform

The integration of the two-dimensional discrete Fourier Transform (2D DFT) into the P²GCL framework is crucial for capturing the global characteristics of atmospheric turbulence effects in imaging. This is because atmospheric turbulence can be modeled as a series of random phase delays following the phase screen propagation theory[26]. The split-step propagation equation is given by:

$$E(z + \Delta z, x, y) \approx \mathcal{F}^{-1} \{ \exp(ik_z \Delta z) \cdot \mathcal{F} [\exp(i\phi(x, y)) \cdot E(z, x, y)] \}, \quad (10)$$

where $E(z, x, y)$ is the complex light field amplitude at propagation distance z , Δz is the propagation step size, k_z is the longitudinal wave number, $\phi(x, y)$ represents the phase screen, and \mathcal{F} and \mathcal{F}^{-1} denote the forward and inverse Fourier transforms, respectively. These phase fluctuations modulate the wavefront of light propagating through the atmosphere, resulting in distortions in the observed image intensity patterns. The 2D DFT allows transforming the image data from the spatial domain to the frequency domain, where the effects of atmospheric turbulence manifest as specific frequency components. The equation for the 2D DFT is:

$$\mathcal{F}(u, v) = \sum_{x=0}^{M-1} \sum_{y=0}^{N-1} f(x, y) \cdot e^{-i2\pi\left(\frac{ux}{M} + \frac{vy}{N}\right)}, \quad (11)$$

where M and N are the image dimensions in pixels, and u and v represent the spatial frequency variables. In addition, accumulating all pixels endows each element in the frequency domain with global awareness of the pixels. Through this transformation, the P²GCL framework gains the ability to analyze the frequency spectrum of turbulence-degraded images, enabling a more comprehensive understanding of how different turbulence scales contribute to the overall distortion effects. This global frequency awareness is crucial for effectively targeting and correcting distortions caused by atmospheric turbulence, as it allows the model to distinguish between areas of the image

that are differently affected by turbulence of varying scales. By leveraging the Fourier Transform in conjunction with the phase screen and diffraction theories, the P²GCL framework attains a physics-inspired perspective, facilitating improved restoration outcomes by focusing on correcting both the global and local effects of turbulence within the frequency domain.

5.2. C_n^2 -Guided Training Strategy

The training process of P²GCL is illustrated in Fig.1, where the core idea is the cooperative learning guided by physical prior between TRNet and TMNet. When training TRNet, the degraded image sequence first passes through TMNet to estimate TS parameters, including $[C_n^2, C_T^2, T]$, as shown in Fig.1(a). Then, these TS parameters are fed into TRNet as the prompt. Meanwhile, the 2D refractive index structure constant matrix C_n^2 is extracted separately and upsampled by a factor of 16. This up-sampled matrix acts as an physical prior and guides the training of TRNet. The C_n^2 matrix represents 2D TS. To make TRNet focus on the areas that are more severely affected by turbulence during training, we propose a C_n^2 -guided frequency loss function $L_{C_n^2}$:

$$L_{C_n^2} = \left\| \mathcal{F}(C_n^2 \odot S_{rest}) - \mathcal{F}(C_n^2 \odot S_{gt}) \right\|_m, \quad (12)$$

where $\|\cdot\|_m$ represents the Manhattan norm of a complex matrix, S_{gt} is the ground truth of S_{rest} and \odot denotes element-wise multiplication of matrices. In the regions within S_{turb} that are highly affected by turbulence, the value of C_n^2 tends to be larger. Hence, C_n^2 is used to weight S_{rest} and S_{gt} , allocating greater weight to areas with more severe degradation. Additionally, the Fourier Transform \mathcal{F} is introduced to endow the network with global awareness. This combination allows the network to adaptively sense local details while still taking into account global information during the training process. To enable C_n^2 guidance to take advantage of the benefits of thermal infrared imaging, we introduce a physical constraint on C_n^2 when training TMNet. According to Eq.2, the physical constraint loss function L_{physic} can be expressed as:

$$L_{physic} = \mathbb{E} \left(C_n^2 - \left(k \frac{P}{T^2} \right)^2 C_T^2 \right). \quad (13)$$

where $\mathbb{E}(\cdot)$ denotes mathematical expectation. In addition, the C_n^2 , C_T^2 , and T are subjected to supervision with their corresponding ground truth matrices.

The loss function can be written as:

$$L_p = \mathbb{E}(\|C_T^2 - \hat{C}_T^2\|_1 + \|T - \hat{T}\|_1 + \|C_n^2 - \hat{C}_n^2\|_1), \quad (14)$$

where $\|\cdot\|_1$ stand for L_1 regularization, \hat{C}_n^2 , \hat{C}_T^2 , \hat{T} represents the ground truth matrix. The TRNet is also trained using both L_1 regularization loss and perceptual loss. The L_1 loss function and the $L_{perceptual}$ loss function[27] can be expressed as:

$$L_1 = \|S_{rest} - S_{gt}\|_1, \quad (15)$$

$$L_{perceptual} = \|G_{vgg}(S_{rest}) - G_{vgg}(S_{gt})\|_1, \quad (16)$$

where G_{vgg} represents VGG19’s first 35 feature layers[27]. The entire loss function for training PBCL can be expressed as:

$$\begin{cases} L_{TRNet} = L_1 + \lambda_1 L_{perceptual} + \lambda_2 L_{C_n^2}, \\ L_{TMNet} = L_p + \lambda_3 L_{physic}, \end{cases} \quad (17)$$

where λ_1 , λ_2 , λ_3 are the weights of the loss function. During each training iteration, the TRNet and TMNet are trained alternatively. This process starts with TRNet, which receives the predicted physical prior O_{TS} generated by TMNet in a single input mode. The coordinate attention block[6] receives the physical prior O_{TS} . Under the supervision of S_{gt} , TRNet’s parameters are updated using gradients from L_{TRNet} during backpropagation. At this step, the parameters of TMNet remain unchanged. In the next step, TMNet is trained. The clear image sequences produced by TRNet are passed through the data mixing block. This block ensures an even distribution of training data by feeding only half of the data to TMNet, guaranteeing a balanced 1:1 mixed training approach between the single and dual input modes. The parameters of TRNet remain unchanged, and TMNet gets the gradient from L_{TMNet} to update its own parameters. In the training strategy above, the $L_{C_n^2}$ we designed guides TRNet to learn in a physically meaningful direction, and forms a collaborative relationship with L_{physic} , L_p . The mixed data training allows TMNet to generalize across different modes and avoids using two separate blocks to accomplish the same task.

6. Dataset

Training data used the Turbulence-Distorted Infrared Imaging Dataset (TIID) [28]. The TIID was captured using a FLIR-A615 thermal infrared

camera equipped with a 100 mm telephoto lens, sensitive to mid-long-wave infrared light in the 8-13 μ m range. The dataset includes algorithm-simulated data for both model training and testing, as well as real-world recorded data. The algorithm-simulated data contained 106,500 frames and 5,702 sequences with corresponding 2D TS fields (C_n^2 and C_T^2). The simulated data had a resolution of 640 \times 480 pixels. For training, there were 4,598 sequences with a sequence length of 15 frames. For testing, there were 1,104 sequences with sequence lengths ranging from 15 to 1,240 frames. Each sequence in the simulated data was divided into 16 \times 16 pixel blocks, with different turbulence quantities (C_n^2 , temperature T , and C_T^2) set for each block. The C_n^2 values were randomly sampled from 0 to $6 \times 10^{-12} m^{-2/3}$, and temperatures T from 298.15K to 320K, with C_T^2 calculated based on C_n^2 and T . This allowed the turbulence quantities to have random 2D spatial distributions resembling real atmospheric turbulence.

7. Experiments and results

7.1. Implementation Details

The PBCL model was trained on the Turbulence-Distorted Infrared Imaging Dataset (TIID) [28] using PyTorch. The training was performed on a RTX 3090 GPU for 100 epochs with a batch size of 2. The AdamW optimizer was employed with an initial learning rate of 10^{-4} , along with a cosine annealing restart scheduler with periods [8, 92], restart weights [1, 1], and minimum learning rates [0.0003, 0.000001]. The loss function for the TRNet consisted of an L_1 loss with a weight of 1.0 and a perceptual loss with a weight of 0.001. For the TMNet, an L_p loss with a weight of 1.0 and a physical constraint loss with a weight of 0.01 were used. Additionally, a C_n^2 -guided frequency loss weighted by 0.001 was incorporated to guide the TIM using the measured C_n^2 values.

7.2. Experimental Results

We present the quantitative and qualitative evaluation of our proposed P²GCL framework against several methods for the task of inhibiting turbulence effects and restoring the quality of infrared images. Our experimental results are systematically summarized in Tables 1 and 2, followed by a visual comparison in Figures 3, 4 and 5. Through the experimental results, the P²GCL framework’s excellence extends to the precise and reliable estimation of TS, where it significantly outshines the PBCL method with lower

MAE and RMSE values and higher R-squared(R^2) scores. This improvement indicates a more accurate and dependable TS measurement, crucial for applications in atmospheric science and remote sensing. Notably, for C_n^2 , P²GCL improves the MAE by 0.0156 and enhances the R^2 score by 0.1065 compared to PBCL, underlining its enhanced predictive capability over PBCL.

Table 1: Comparison of the accuracy of TS measurements. The symbols \uparrow and \downarrow indicate better performance with higher and lower values, respectively. The best results are highlighted in bold.

Method	TS MAE (\downarrow)	RMSE (\downarrow)	MSLE (\downarrow)	R^2 (\uparrow)
Unet[29]	C_n^2 0.0614	0.0903	0.0078	0.5347
	C_T^2 0.0544	0.0816	0.0067	0.5311
GRCNN[30]	C_n^2 0.1187	0.1633	0.0286	< 0.1
	C_T^2 0.1027	0.1439	0.0235	< 0.1
PBCL[6]	C_n^2 0.0387	0.0569	0.0027	0.8233
	C_T^2 0.0345	0.0509	0.0022	0.8274
P ² GCL	C_n^2 0.0231	0.0357	0.0011	0.9298
	C_T^2 0.0205	0.0324	0.0010	0.9279

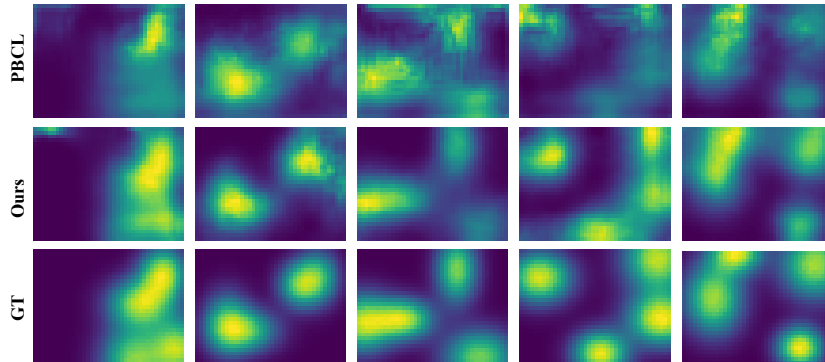


Figure 3: Visualization of TS measurement. The results of the PBCL method, our P²GCL method, and the ground truth (GT) are displayed in rows for comparison across different scenes.

Figure 3 visually demonstrates the performance of our P²GCL framework in measuring TS, in comparison to the PBCL method and the ground truth. The representations produced by our method show a marked improvement

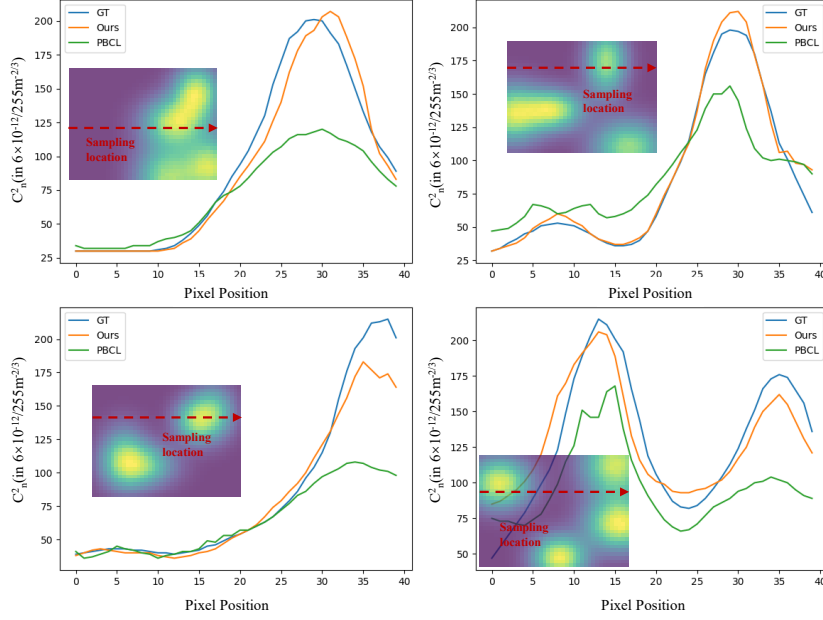


Figure 4: TS value visualization. Comparison across GT, PBCL, and P²GCL methods, with sampling locations indicated on the heat maps.

in matching the ground truth’s intensity patterns of TS. The results exhibit less noise and more distinct feature resolution, which corroborates the quantitative advancements in our method’s MAE and R^2 metrics over PBCL. In Fig.4, TS values are plotted against pixel positions, showing the performance of GT, PBCL, and P²GCL. Insets highlight where measurements were taken. The P²GCL closely aligns with GT, suggesting higher measurement accuracy. This visual assessment complements the quantitative findings, emphasizing the substantial progress achieved by P²GCL in TS measurement accuracy.

Additionally, the P²GCL framework outperforms existing methods in the mitigation of turbulence effects and the restoration of infrared image quality, as quantitatively demonstrated in Tab. 2. The P²GCL framework achieves the lowest NRMSE and the highest PSNR, SSIM, and VI scores among the evaluated methods. The visual results presented in Fig.5 further substantiate the efficacy of our P²GCL framework. While the improvement in image restoration might not be immediately discernible in still images, it becomes evident when observing video sequences.

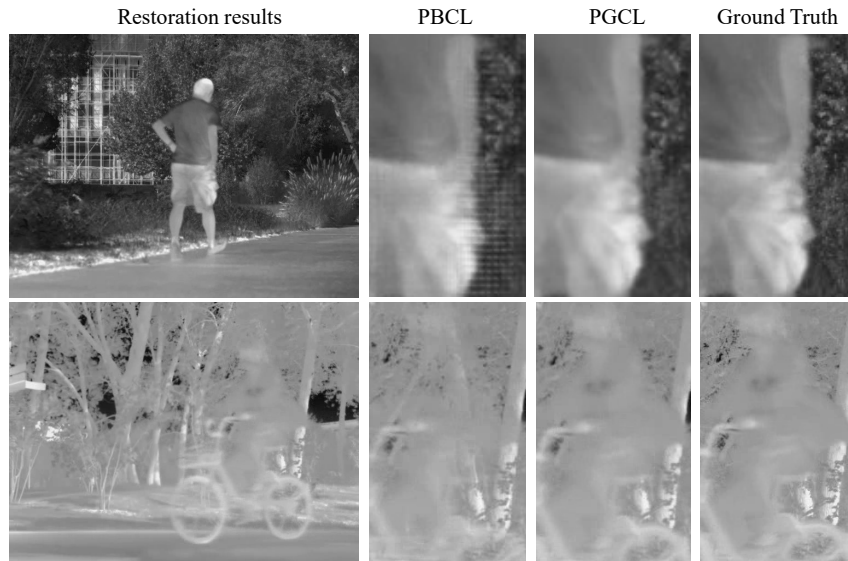


Figure 5: Visualization of infrared image restoration results. Please refer to the supplementary materials for the restoration results of simulated and real degraded videos.

Table 2: Quantitative results of inhibiting turbulence effects. The symbols \uparrow and \downarrow indicate better performance with higher and lower values, respectively. The best results are highlighted in bold.

Method	NRMSE (\downarrow)	PSNR (\uparrow)	SSIM (\uparrow)	VI (\downarrow)
ESTRNN[31]	0.0399	33.6251	0.9417	6.3276
MIRNet[32]	0.0555	30.5494	0.9133	6.8996
BasicVSR[33]	0.0462	32.3566	0.9187	6.9768
TSR-WGAN[11]	0.0543	30.6246	0.9310	6.3968
PBCL[6]	0.0316	35.7363	0.9484	6.0804
P ² GCL	0.0308	36.0138	0.9487	6.0787

7.3. Ablation study

In the ablation study detailed in Tab.3, the PSNR and R^2 metrics significantly inform the efficacy of the P²GCL framework. The full P²GCL configuration achieves the highest PSNR value, suggesting superior image restoration quality. Similarly, the complete framework attains the best R^2 scores, indicating the most accurate TS measurements. The absence of the physical constraint loss function L_{physic} leads to a discernible decrease in

both PSNR and R^2 , while removing the C_n^2 -guided frequency loss function $L_{C_n^2}$ results in more substantial performance drops. The substitution with the Original Reconstructor, compared to the transformer-based model, presents a reduction in both metrics, emphasizing the transformer’s superior capabilities. Lastly, the exclusion of the Data Mixing block has a moderate impact, yet reaffirms its contribution to the framework’s robustness.

Table 3: Ablation study results for P²GCL. The symbol “-” indicates the omission of a component, with “-Transformer reconstructor” indicating the replacement of the Transformer reconstructor with the Original Reconstructor. The best results are highlighted in bold.

Configuration	PSNR (\uparrow)	$R^2 (C_n^2)$ (\uparrow)	$R^2 (C_T^2)$ (\uparrow)
Full P²GCL	36.0138	0.9298	0.9279
- L_{physic}	35.7304	0.9214	0.9177
- $L_{C_n^2}$	35.6558	0.9158	0.9015
- Transformer reconstructor	35.4097	0.8943	0.8883
- Data Mixing Block	35.9382	0.9063	0.9003

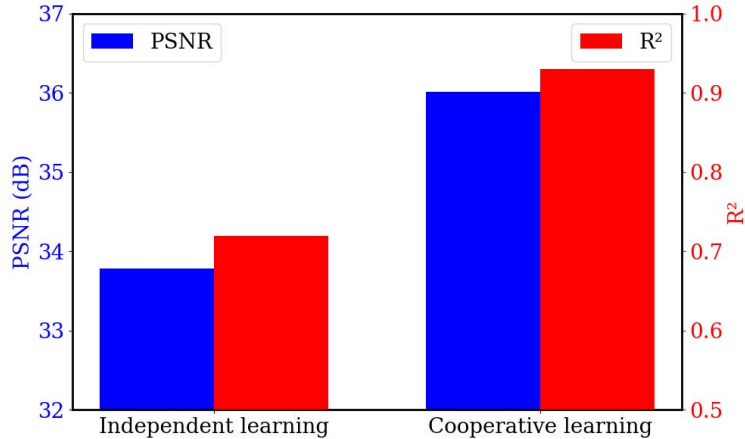


Figure 6: Comparison between cooperative and independent learning.

The experiment results that compared cooperative learning and independent learning in a quantitative form are presented in Fig.6. Independent learning involves isolated training of TMNet and TRNet, without guidance

from $L_{C_n^2}$ and data mixing block. Cooperative learning is their joint training under the P²GCL framework. The results showed an improvement in the P²GCL approach, with a 36.01dB compared to 33.78dB in independent learning. This indicates a 2.23dB increase in PSNR, implying higher quality image restoration with the cooperative approach. The R^2 value, which is a statistical measure indicating the accuracy of turbulence estimation, was used. The results showed that P²GCL scored 0.9298 while independent learning scored 0.7195, indicating an improvement of 0.2103.

8. Conclusion and Limitation

This paper presents the P²GCL framework that combines physical priors with cooperative learning for atmospheric TS estimation and infrared image restoration. In P²GCL, TMNet generates TS predictions to guide TRNet’s image restoration, while TRNet’s restored reference images in turn enhance TMNet’s measurement accuracy. With the C_n^2 -guided frequency loss and physical constraint loss, the framework effectively incorporates physical principles into the training process. Compared to existing methods, P²GCL exhibits superior performance across multiple evaluation metrics, verifying the effectiveness of the cooperative learning strategy. Despite achieving state-of-the-art C_n^2 MAE of 0.0231 and R^2 of 0.9298 for turbulence estimation, along with a leading PSNR of 36.0138 dB for image restoration, there is still room for continued improvement and generalization of the framework. In the future, we expect to extend this framework to other imaging modalities to further broaden its application prospects. Although currently focused on thermal infrared imaging, applying P²GCL to visible light or event camera could further amplify its impact.

References

- [1] X. Dai, X. Yuan, X. Wei, Tirnet: Object detection in thermal infrared images for autonomous driving, *Applied Intelligence* 51 (2021) 1244–1261.
- [2] M. Yang, W. Xu, Z. Sun, H. Wu, Y. Tian, L. Li, Mid-wave infrared polarization imaging system for detecting moving scene, *Optics Letters* 45 (20) (2020) 5884–5887.

- [3] N. Hu, H. Song, R. Zhang, H. Zhou, C. Liu, X. Su, H. Song, K. Pang, K. Zou, B. Lynn, et al., Demonstration of turbulence mitigation in a 200-gbit/s orbital-angular-momentum multiplexed free-space optical link using simple power measurements for determining the modal crosstalk matrix, *Optics Letters* 47 (14) (2022) 3539–3542.
- [4] F. Cantalloube, J. Milli, C. Böhm, S. Crewell, J. Navarrete, K. Rehfeld, M. Sarazin, A. Sommani, The impact of climate change on astronomical observations, *Nature Astronomy* 4 (9) (2020) 826–829.
- [5] X. Li, Endurance of unmanned aerial vehicles, *SCIENTIA SINICA Informationis* (2023).
URL <https://api.semanticscholar.org/CorpusID:259489266>
- [6] Y. Wang, D. Jin, J. Chen, X. Bai, Revelation of hidden 2d atmospheric turbulence strength fields from turbulence effects in infrared imaging, *Nature Computational Science* 3 (8) (2023) 687–699.
- [7] K. Browning, C. Watkins, Observations of clear air turbulence by high power radar, *Nature* 227 (5255) (1970) 260–263.
- [8] H. Zhou, X. Su, Y. Duan, H. Song, K. Zou, R. Zhang, H. Song, N. Hu, M. Tur, A. E. Willner, Atmospheric turbulence strength distribution along a propagation path probed by longitudinally structured optical beams, *Nature Communications* 14 (1) (2023) 4701.
- [9] S. Wu, X. Hu, Y. Han, X. Wu, C. Su, T. Luo, X. Li, Measurement and analysis of atmospheric optical turbulence in lhasa based on thermosonde, *Journal of Atmospheric and Solar-Terrestrial Physics* 201 (2020) 105241.
- [10] S. Gao, X. Liu, Y. Chen, J. Jiang, Y. Liu, Y. Jiang, Atmospheric turbulence strength estimation using convolution neural network, *IEEE Photonics Journal* (2023).
- [11] D. Jin, Y. Chen, Y. Lu, J. Chen, P. Wang, Z. Liu, S. Guo, X. Bai, Neutralizing the impact of atmospheric turbulence on complex scene imaging via deep learning, *Nature Machine Intelligence* 3 (10) (2021) 876–884.

- [12] Z. Zhang, B. Zhao, Y. Chen, Z. Wang, D. Wang, J. Sun, J. Zhang, Z. Xu, X. Li, Asf-transformer: neutralizing the impact of atmospheric turbulence on optical imaging through alternating learning in the spatial and frequency domains, *Optics Express* 31 (22) (2023) 37128–37141.
- [13] D. Ren, K. Zhang, Q. Wang, Q. Hu, W. Zuo, Neural blind deconvolution using deep priors, in: *Proceedings of the IEEE/CVF Conference on Computer Vision and Pattern Recognition*, 2020, pp. 3341–3350.
- [14] Q. Lyu, H. Shan, G. Wang, Mri super-resolution with ensemble learning and complementary priors, *IEEE Transactions on Computational Imaging* 6 (2020) 615–624.
- [15] Q. Guo, S. Gao, X. Zhang, Y. Yin, C. Zhang, Patch-based image inpainting via two-stage low rank approximation, *IEEE transactions on visualization and computer graphics* 24 (6) (2017) 2023–2036.
- [16] Y. Huang, S. Li, L. Wang, T. Tan, et al., Unfolding the alternating optimization for blind super resolution, *Advances in Neural Information Processing Systems* 33 (2020) 5632–5643.
- [17] Y. Liu, J. Pan, J. Ren, Z. Su, Learning deep priors for image dehazing, in: *Proceedings of the IEEE/CVF international conference on computer vision*, 2019, pp. 2492–2500.
- [18] Q. Yi, J. Li, Q. Dai, F. Fang, G. Zhang, T. Zeng, Structure-preserving deraining with residue channel prior guidance, in: *Proceedings of the IEEE/CVF International Conference on Computer Vision*, 2021, pp. 4238–4247.
- [19] X. Zhu, P. Milanfar, Removing atmospheric turbulence via space-invariant deconvolution, *IEEE transactions on pattern analysis and machine intelligence* 35 (1) (2012) 157–170.
- [20] Z. Mao, A. Jaiswal, Z. Wang, S. H. Chan, Single frame atmospheric turbulence mitigation: A benchmark study and a new physics-inspired transformer model, in: *European Conference on Computer Vision*, Springer, 2022, pp. 430–446.

- [21] S. N. Rai, C. Jawahar, Removing atmospheric turbulence via deep adversarial learning, *IEEE Transactions on Image Processing* 31 (2022) 2633–2646.
- [22] X. Zhang, Z. Mao, N. Chimitt, S. H. Chan, Imaging through the atmosphere using turbulence mitigation transformer, *IEEE Transactions on Computational Imaging* (2024).
- [23] A. Jaiswal, X. Zhang, S. H. Chan, Z. Wang, Physics-driven turbulence image restoration with stochastic refinement, in: *Proceedings of the IEEE/CVF International Conference on Computer Vision, 2023*, pp. 12170–12181.
- [24] Z. Mao, N. Chimitt, S. H. Chan, Accelerating atmospheric turbulence simulation via learned phase-to-space transform, in: *Proceedings of the IEEE/CVF International Conference on Computer Vision, 2021*, pp. 14759–14768.
- [25] J. Liu, P. Wang, X. Zhang, Y. He, X. Zhou, H. Ye, Y. Li, S. Xu, S. Chen, D. Fan, Deep learning based atmospheric turbulence compensation for orbital angular momentum beam distortion and communication, *Optics express* 27 (12) (2019) 16671–16688.
- [26] N. A. Roddier, Atmospheric wavefront simulation using zernike polynomials, *Optical engineering* 29 (10) (1990) 1174–1180.
- [27] J. Johnson, A. Alahi, L. Fei-Fei, Perceptual losses for real-time style transfer and super-resolution, in: *ECCV, 2016*, pp. 694–711.
- [28] Y. Wang, Turbulence-distorted infrared imaging dataset, <https://zenodo.org/records/8002688> (2022).
URL <https://zenodo.org/records/8002688>
- [29] O. Ronneberger, P. Fischer, T. Brox, U-net: Convolutional networks for biomedical image segmentation, in: *Medical Image Computing and Computer-Assisted Intervention–MICCAI 2015: 18th International Conference, Munich, Germany, October 5-9, 2015, Proceedings, Part III* 18, Springer, 2015, pp. 234–241.

- [30] J. Wang, X. Hu, Convolutional neural networks with gated recurrent connections, *IEEE Transactions on Pattern Analysis and Machine Intelligence* 44 (7) (2021) 3421–3435.
- [31] Z. Zhong, Y. Gao, Y. Zheng, B. Zheng, Efficient spatio-temporal recurrent neural network for video deblurring, in: *Computer Vision–ECCV 2020: 16th European Conference, Glasgow, UK, August 23–28, 2020, Proceedings, Part VI 16*, Springer, 2020, pp. 191–207.
- [32] S. W. Zamir, A. Arora, S. Khan, M. Hayat, F. S. Khan, M.-H. Yang, L. Shao, Learning enriched features for real image restoration and enhancement, in: *Computer Vision–ECCV 2020: 16th European Conference, Glasgow, UK, August 23–28, 2020, Proceedings, Part XXV 16*, Springer, 2020, pp. 492–511.
- [33] K. C. Chan, X. Wang, K. Yu, C. Dong, C. C. Loy, Basicvsr: The search for essential components in video super-resolution and beyond, in: *CVPR*, 2021, pp. 4947–4956.